A. Schwanke; RB; Wittee Lopes, C.; Debora Motta Meira; Díaz Morales, UM.; Sibele B. Pergher; Katia Bernardo-Gusmao (2021). Structure and reactive properties of Nb-impregnated two-dimensional pillared MWW zeolites for total oxidation of volatile organic compounds. Microporous and Mesoporous Materials. 327:1-11. https://doi.org/10.1016/j.micromeso.2021.111425

Nb-impregnated two-dimensional pillared MWW zeolites for oxidative abatement of volatile organic compounds.

Anderson Joel Schwanke [a*], Rosana Balzer [b], Christian Wittee Lopes [a], Débora Motta Meira [c,d], Urbano Díaz [e], Sibele Pergher [f], Katia Bernardo-Gusmão [a]

[a] Universidade Federal do Rio Grande do Sul, 91501-970, Porto Alegre, RS, Brasil.
*Corresponding author: anderson-js@live.com

[b] Universidade Federal do Paraná - UFPR, 85950-000, Palotina, PR, Brasil.

[c] CLS@APS, Advanced Photon Source, Argonne National Laboratory, 9700 S. Cass Avenue, Argonne, IL 60439, USA.

[d] Canadian Light Source Inc., 44 Innovation Boulevard, Saskatoon, Saskatchewan S7N 2V3, Canada.

[e] Instituto de Tecnología Química, Universitat Politècnica de València-Consejo Superior de Investigaciones Científicas, Avenida de los Naranjos s/n, 46022 Valencia, Spain.

[f] Universidade Federal do Rio Grande do Norte - UFRN, 59078-970, Natal, RN, Brasil.

ABSTRACT

In this work, the structure and reactive properties of Nb-impregnated MWW-type materials were evaluated for the gas phase total oxidation of volatile organic compounds (VOC), including benzene, toluene, and o-xylene (BTX). The role of the type of structure (two or three-dimensional) and the loading of Nb were considered. The results indicated most Nb species with tetrahedral coordination on the external surfaces of both 2D and 3D zeolites, together with a minimal contribution of octahedral extra-framework Nb_2O_5 species. The texture and Nb content played a key role in the gas phase total oxidation of BTX. With the same Nb content (5 wt%), the pillared zeolite exhibited a higher specific surface, larger pore volume, and mesopores between the MWW nanosheets when compared to the MCM-22 zeolites, which resulted in high accessibility of the reactant molecules to the active sites, and reflected in higher BTX conversion at lower and higher temperatures (50 - 300 °C). The best performance was achieved with the pillared zeolite (10 wt% of Nb), reaching BTX conversion at 300 °C of 92, 69, and 58%, respectively. The catalyst was stable up to 30 h of reaction.

1. INTRODUCTION

Zeolites are crystalline microporous materials build-up of atoms tetrahedrally coordinated by oxygen atoms (SiO_4, AlO_4^-, specially) coordinated by oxygen atoms. There are more than 250 different zeolite topologies up to now. They possess cavities and channels with sizes of ca. 1 nm, able to accommodate/release charge balancing cations and molecules [1]. Consequently, their properties include shape selectivity, ion exchanging ability, high surface area, tunable chemical composition and acidity, and zeolites, which are widely applied as supports, ion exchangers, molecular sieves, and catalysts [2].

Zeolites with MWW code are an example of the successful materials exploited industrially with the three-dimensional MCM-22 zeolite being applied in the Mobil/Badger cumene process [3]. This framework topology has P6/mmm hexagonal crystal system, a framework density of 15.9 Tetrahedra/1000 $Å^3$, and *d6r* and *mel* composite building formed units. The pore system comprises medium- and large-pores formed by ten-ring sinusoidal channels with 0.40 x 0.50 nm, and ten-ring bidirectional channels with 0.40 x 0.55 nm. Another pore system comprises twelve-ring supercavities with an internal height and internal diameter of 1.81 and 0.71 nm, respectively. Double six-rings interconnect these supercavities along the *c* axis [1].

Other successful MWW-type materials were obtained after discovering that MCM-22 zeolite passes through a two-dimensional (2D) precursor before condensation of nanosheets through calcination [4]. The intercalation of surfactant molecules allows to obtain novel materials with high surface area and combined micro/mesopores through the separation of MWW nanosheets (thickness of 2.5 nm), exposing their active sites located in the 12-ring hemicavities, e.g. ITQ-2 (delaminated) [5], MCM-56 (disordered) [6], and MCM-36 (pillared) [7].

Originally, the MCM-36 was synthesized using a mixture of the surfactant intercalated 2D precursor and a silicon alkoxide solution (TEOS) as a pillaring agent. After calcination, amorphous SiO_2 pillars create interlayer galleries with the retention of MWW nanosheets [7]. The MCM-36 with SiO_2 pillars was applied in acid-catalysed reactions as well as those involving large substrate molecules [7-8]. The possibility of inserting heteroatoms in pillared zeolites combined with their high surface area, interlayer accessibility, and well dispersion of the active sites wides the range of application for other reactions. To date, studies on the effect of heteroatoms in MWW-type pillared

materials are still scarce and more efforts to understand the nature of pillars are desirable [9].

Two main approaches describe the introduction of heteroatoms in MWW-type pillared zeolites: (i) including the metal source into the pillaring solution, (ii) loading the metal by impregnation methods (e.g. wetness impregnation) on the as made pillared zeolite. The first one comprises the use of a pillaring solution with mixed salts/oxides of the desired elements under an alkaline medium, originally reported by Lercher et al. to obtain acid-base properties using MCM-36 with Al-Mg, Ba-Al, Mg-Al-Si, or Ba-Al-Si oxide pillars applied on the reduction of nitrogen oxides from FCC regenerator flue gas streams [10]. Afterward, efforts were dedicated to understanding if the heteroatoms were isomorphically substituted into the pillars or occupying non-framework positions, especially for redox and acid-redox reactions. The examples include the use of alkoxides mixtures including TEOS and tetrabutylorthotitanate (TBOT) to obtain Si/Ti-pillared MCM-36 for epoxidation [11], TBOT to obtain pure Ti pillared MCM-36 for the CO_2 capture [12], a mixture of TEOS and Nb ethoxide to obtain MCM-36 with pillars of niobiosilicate for liquid-phase oxidation of cyclohexene and methylene blue [13]. Recently, our group reported MCM-36 with Si/Nb oxide pillars using TEOS and Nb ethoxide, applied for the gas-phase total oxidation of volatile organic compounds (VOC), including BTX [14].

Regarding the metals-impregnated in MCM-36, examples include Au supported on the titanosilicate pillared MCM-36 for epoxidation [15], V supported MCM-36 for oxidative dehydrogenation [16], Pt supported MCM-36 for dealkylation and transalkylation [17], Zn, Au, Ag, Au-Zn, Ag-Zn, and AuAg-Zn supported MCM-36 for methanol oxidation [18]. So far, no studies have been dedicated to the synthesis and catalytic behavior of Nb-impregnated MCM-36 materials.

To date, several efforts have been realized to minimize VOC emission, and BTX are an example of VOC that exhibits harmful effects on the environment and human health [19]. Among the current technologies, the catalytic oxidation of VOC is the most suitable because it allows operating under mild reaction conditions without creating toxic by-products. Moreover, the searching for alternative catalysts to those based on expensive noble metals e.g. Pd, Au, Pt, has been directing the research towards the use of noble-metal free catalysts e.g. Mn, Cr, Co, and Ni oxides, dispersed on supports with high surface and large pore volumes [20].

The synthesis of Nb-supported materials for the redox reactions has been gaining prominence because of their combined properties, including acidity, stability, hydrophobicity, and strong metal-support interaction. However, the conditions of preparation, the Nb source, and the type of the final support has a profound influence on the physicochemical and reactive properties [21]. Regarding the Nb-impregnated catalysts for BTX oxidation, no studies have been reported so far. The present communication explores the synthesis of Nb-impregnated MCM-36, and its catalytic behavior for the gas-phase oxidation of BTX.

2. EXPERIMENTAL

2.1 Synthesis and swelling of the MCM-22 precursor: The synthesis was done according to the traditional procedure reported in the literature [22]. The gel (Si/Al = 25) was prepared using SiO_2, $NaAlO_2$, hexamethyleneimine, NaOH, and distilled water. The crystallization was performed at 135 °C, 7 days of crystallization, and under tumbling of the autoclaves (60 rpm). The surfactant intercalation was done at 25 °C for 18 h, and using a solution of hexadecyltrimethylammonium bromide (29 wt%) partially exchanged by OH^- ions with a resin, and a cake (20 wt% of MCM-22P in distilled water) with a weight ratio surfactant solution/cake = 10. After, the basicity was decreased until it reaches pH = 9, using cycles of washing with distilled water.

2.2 Obtaining the MCM-36: Pillaring was done using a weight ratio of the pillaring agent (tetraethyl orthosilicate, TEOS) and the intercalated precursor of 5. The mixture was maintained under N_2 atmosphere and reflux condenser system at 80 °C for 1 day. After the controlled hydrolysis or TEOS, the solid was dried at 40 °C overnight. The calcination was done using a borosilicate tube reactor, at 550 °C (heating rate of 3 °C min^{-1}) under nitrogen flowing, followed by an additional 8 h under oxygen flowing. The MCM-22 precursor was calcined in a muffle furnace at 580 °C for 12 h.

To obtain the acidic (H) materials, MCM-36 and the MCM-22 were ion-exchanged for 3 h at 25 °C, and using an aqueous solution of NH_4NO_3 (0.1 mol L^{-1}), with a weight ratio solution/solid = 50. This procedure was repeated three times. After, the materials were calcined at 500 °C (heating rate of 5 °C min^{-1}) for 2 h under air atmosphere.

2.3 Niobium impregnation: The Nb impregnation procedure was done similar to the literature [23]. The HMCM-36, was first evaporated for 1 h within a flask connected to the rotary vacuum evaporator. After, an aqueous solution of niobium ammonium oxalate hydrated (5 and 10 wt% of Nb) was added and then evaporated at 80

°C for 4 h. After, the material was dried in an oven at 100 °C for overnight. The same procedure was done with the HMCM-22 using an aqueous solution containing 5 wt% of Nb. The materials were calcined at 500 °C (heating rate of 1 °C min^{-1}) for 4 h. The materials were named according to the wt% of Nb impregnated, $Nb_{0.05}$/HMCM-36, $Nb_{0.1}$/HMCM-36, and $Nb_{0.05}$/HMCM-22. Niobium oxide (Nb_2O_5) was used as a reference.

2.4 Oxidation of benzene, toluene and *o*-xylene: The conditions were: 30 mg catalyst; benzene (1300 mg m^{-3}), toluene (700 mg m^{-3}), and o-xylene (600 mg m^{-3}) added to air; gas flow rate of 0.33 cm^3 s^{-1}; residence time of 0.3 s; space velocity of 12000 $mL.g^{-1}$ h^{-1}; and temperature range of between 50 and 300 °C. It was used a quartz reactor under atmospheric pressure. The data were collected after 2 h on-stream at room temperature and the products were determined with a GC-MS. The substrate and product mixtures were analyzed using two online gas chromatographs. The conversion of BTX follows:

$$\text{Conv. (\%)}: \frac{Xinput - Xoutput}{Xinput} \cdot 100$$

Where *X* represents benzene, toluene or o-xylene.

The reactants were purchased from Evonik (SiO_2 aerosil 200), Sigma-Aldrich (NaOH 98%, HMI 98%, TEOS 98%, $C_{16}TABr$, NH_4NO_3, $C_4H_4NNbO_9 \cdot xH_2O$ 99.99 %), Riedel-de-Haen ($NaAlO_2$, 40-45% Al_2O_3), Amberlite (resin IRN-78), Alfa Aesar (Nb_2O_5 99.9 %), and Vetec (benzene 99.5%, toluene 99.5%, o-xylene 98%).

Characterization: The crystalline structure of samples was verified by a Rigaku (Ultima IV model) diffractometer using Cu-Kα1 with a step size of 0.02°.

Field-Emission Scanning Electron Microscopy (FESEM) analyses were obtained on ZEISS Ultra 55 microscope operating at 2 kV. TEM images were obtained on a JEOL FEM 2100F operating at 200 kV, using bright-field (BF) and high-angle annular dark-field imaging (HAADF) modes.

Nitrogen and argon adsorption isotherms were obtained with a Micromeritics Tristar 3020 and ASAP 2020, respectively. Prior to the measurements, the samples were degassed at 300 °C for 12 h. The BET method [24] was used to calculate the surface area S_{BET} using the adsorption data from p/p^0 = 0.06 to 0.11. The total pore total volume V_{total} was estimated from the amount of N_2 adsorbed at a relative pressure p/p^0 = 0.99. The micropore volume was estimated by the t-plot method. The pore size distribution was estimated using the DFT with slit-like pore model. Infrared (IR) spectroscopy with

adsorption and desorption of pyridine (Py) as probe molecule was performed in Thermo Fischer Scientific, Nicolet 710. Diffuse reflectance UV-Vis spectroscopy was collected on a Varian, Cary 5000. The X-ray photoelectron spectroscopy (XPS) analyses were performed in an Omicron-SPHERA station.

X-ray Absorption Spectroscopy experiments were carried out at Nb K-edge (18986 eV) at the 20 BM beamline of Argonne National Laboratory (Lemont, IL, USA) [25]. The samples were pelletized and the spectra were collected at room temperature in transmission mode employing ionization chambers. Energy calibration was checked by Nb foil placed between I_1 and I_2 ionization chambers. Reference compounds were also measured in order to have a proper comparison with the measured samples. Three scans per sample were acquired to ensure spectral reproducibility. Data treatment has been performed using Athena software implemented in the Demeter package [26].

Solid-state Nuclear Magnetic Resonance spectroscopy (NMR) was performed with a Bruker (model AV 400). ^{27}Al MAS NMR spectra were recorded with a spinning rate of 10 kHz and a 9° pulse length of 0.5 μs with a 1 s repetition time.

3. RESULTS AND DISCUSSION

The XRD patterns of synthesized materials are shown in Figure 1. The HMCM-22 zeolite exhibited (100), (101), (102), (220), and (310) reflections, which are typical of materials with MWW topology [27]. The same reflections remain in the $Nb_{0.05}$/HMCM-22 material, and indicates the niobium impregnation does not alter the crystalline structure of the material. The XRD patterns of HMCM-36, $Nb_{0.05}$/HMCM-36, and $Nb_{0.1}$/HMCM-36 exhibit the same intralayer reflections (100), (220), and (310), indicating that the crystalline structure of the MWW nanosheets remains after pillaring. However, there is a decrease in the intensities of reflections caused by the contribution of amorphous silica. Indeed, Table 1 showed the increase in the Si/Al ratio after pillaring. In addition, the wideband in the region of $2\theta = 8 - 10$ ° between the reflections (101) and (102) is observed and indicates the rupture in the vertical alignment of the stacked MWW nanosheets.

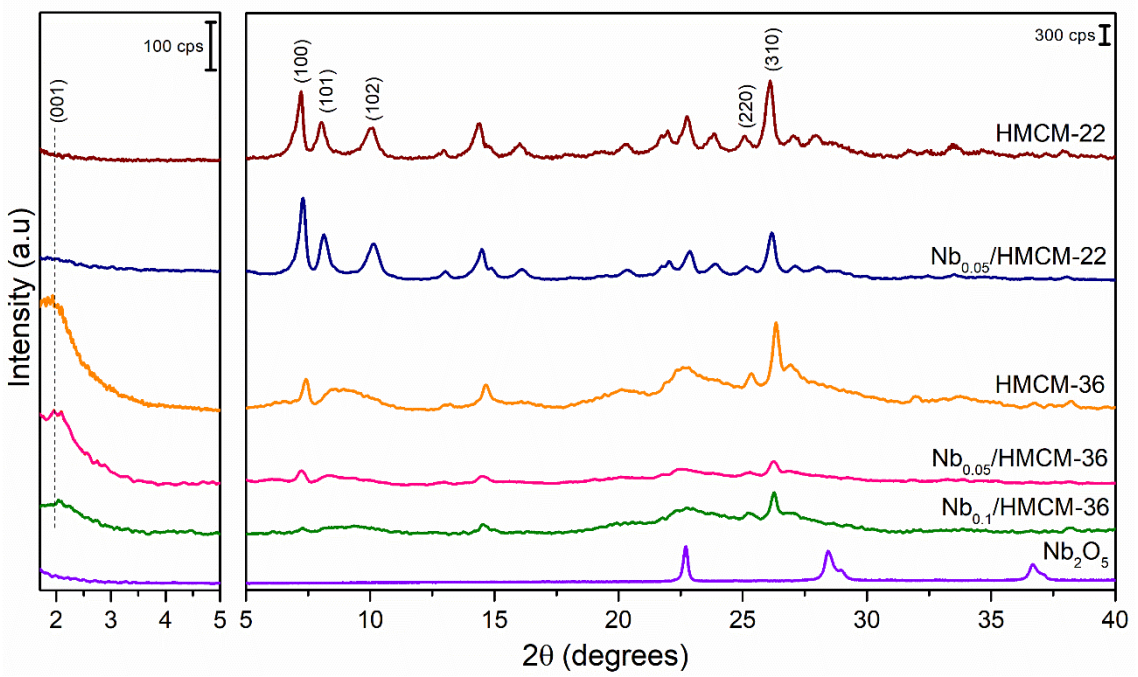

Figure 1. XRD patterns of HMCM-22, $Nb_{0.05}$/HMCM-22, HMCM-36, $Nb_{0.05}$/HMCM-36, $Nb_{0.1}$/HMCM-36 and Nb_2O_5 materials.

Another clear observation that the pillaring was successful was the presence of the interlayer (001) reflection at 2θ = 1.9°, confirming that the separation between the MWW nanosheets was maintained after the niobium impregnation. The d_{001} spacing was 4.6 nm, which subtracted from the thickness of an MWW nanosheet (2.5 nm), was resulted in gallery regions with 2.1 nm heights. The increase in niobium content in pillared material caused the decrease of the intensity of (001) reflection and suggests a decrease in the lamellar stacking order along the *c* axis. Regarding the crystalline phases of niobium, the synthesized materials did not show the reflections at 2θ = 22.6, 28.3, and 36.6°, characteristics of crystalline, probably by the low XRD detection limit or the presence of amorphous Nb_2O_5 phase.

The Nb content in the materials was determined by ICP and indicated in Table 1. For the materials Nb0.05 / HMCM-22, Nb0.05 / HMCM-36, and Nb0.1 / HMCM-36, values of 5.1, 4.2 were obtained and 9.1 wt%, respectively, which are close to the theoretical values.

Table 1. A comparison of physicochemical properties and binding energies (BE) of $Nb_{0.05}$/HMCM-22, $Nb_{0.05}$/HMCM-36 and $Nb_{0.1}$/HMCM-36 materials.

Sample	%Nb [a]	Si/Al [a]	S_{BET} [b]	S_{ext} [b]	V_{micro} [c]	V_{total} [c]	BE (eV) [d]
							Nb 3d5/2
$Nb_{0.05}$/HMCM-22	5.1	24	377	140	0.10	0.34	206.7, 207.6, 210.4
$Nb_{0.05}$/HMCM-36	4.2	36	658	540	0.05	0.55	206.7, 208.2, 210.8, 211.9
$Nb_{0.1}$/HMCM-36	9.1	36	638	515	0.05	0.44	206.2, 207.4, 208.6
Nb_2O_5	--	--	--	--	--	--	207.1

[a] = obtained from ICP, [b] = $m^2\ g^{-1}$, [c] = $cm^3\ g^{-1}$, [d] = obtained from XPS spectra.

To investigate de textural properties of the Nb-impregnated MWW materials, N_2 adsorption isotherms were performed and shown in Figure 2a. The $Nb_{0.05}$/HMCM-22 exhibited a Type-I isotherm at low pressures and characteristic of microporous materials. The gradual increase in the amount of N_2 adsorbed at higher pressures indicates interparticle porosity. For the $Nb_{0.05}$/HMCM-36 and $Nb_{0.1}$/HMCM-36, the increase of N_2 adsorbed at low pressures reveals a strong adsorbent-adsorbate interaction. In addition, the materials have an adsorption step between p/p^0 = 0.12 - 0.4, attributed to the capillary condensation between MWW nanosheets generated by the pillaring. The pore sizes are shown in Figure 2b and reveal that the pillared materials exhibited pore distribution between 1.5 - 3 nm (supermicropores to small mesopores) with a maximum centered at 2.2 nm and near to the height of the galleries between the MWW nanosheets (2.1 nm), as discussed by XRD analysis.

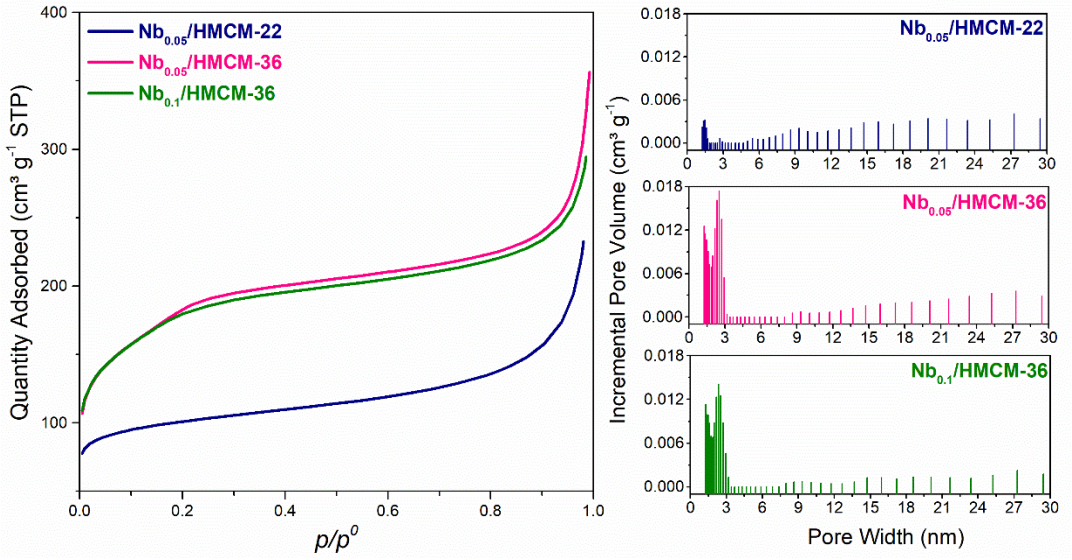

Figure 2. (a) Nitrogen adsorption isotherms and (b) pore widths of $Nb_{0.05}$/HMCM-22, $Nb_{0.05}$/HMCM-36 and $Nb_{0.1}$/HMCM-36 materials.

Table 1 shows the textural properties of the obtained material. In general, the pillared materials exhibited higher values of S_{BET}, S_{ext}, and V_{total} than the 3D zeolite, which was expected due to the pillaring procedure. Regarding the $V_{micro,}$ a decrease of 50% was observed after pillaring and was associated with the separation of the MWW nanosheets. The separation prevents the condensation of silanol groups from adjacent MWW nanosheets, and the formation of the bidirectional pore system of 10-ring members. Furthermore, S_{ext} of the $Nb_{0.05}$/HMCM-36 was 400 m^2 g^{-1} higher than the $Nb_{0.05}$/HMCM-22, and confirms the more exposure of the MWW nanosheets after pillaring.

Regarding the increase in Nb content on the pillared materials, a decrease in S_{ext} was observed, while the V_{micro} remained unchanged, which infers the deposition of Nb occurred on the external surface of MWW nanosheets. Employing accurate analysis with argon of $Nb_{0.05}$/HMCM-36 (see Figure 3) confirmed the combined micro/mesoporous structure. The narrow distribution of micropores at 0.5 nm is attributed to the sinusoidal channels of each MWW nanosheets. The maximum pore sizes between 1.4 - 2.5 nm correspond to the gallery regions between the MWW nanosheets.

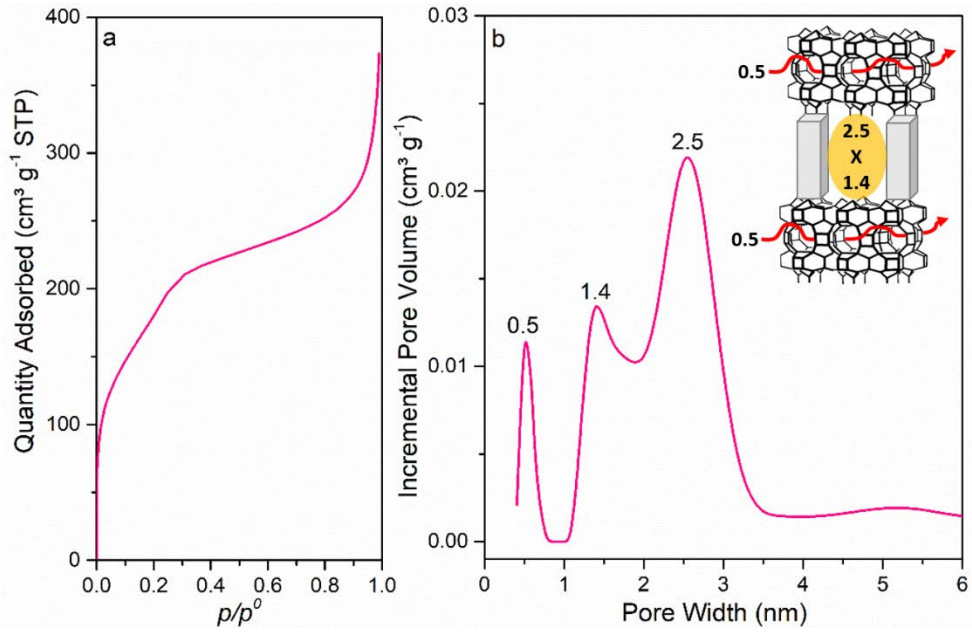

Figure 3. (a) Argon adsorption isotherm and (b) pore width of $Nb_{0.05}$/HMCM-36 material.

The state of niobium was analysed by DR UV-Vis and shown in Figure 4. The spectra reveal bands with high intensities at ~ 210 and ~ 230 nm, assigned as tetrahedral Nb(V) species in the silica structure [23]. Hence, $Nb_{0.05}$/HMCM-22 and $Nb_{0.1}$/HMCM-36

present wider bands in the region of ~300 nm (this widening is more pronounced in $Nb_{0.05}$/HMCM-22); when comparing them to the crystalline Nb_2O_5 sample reference, it suggests the presence of extra-framework octahedral Nb species.

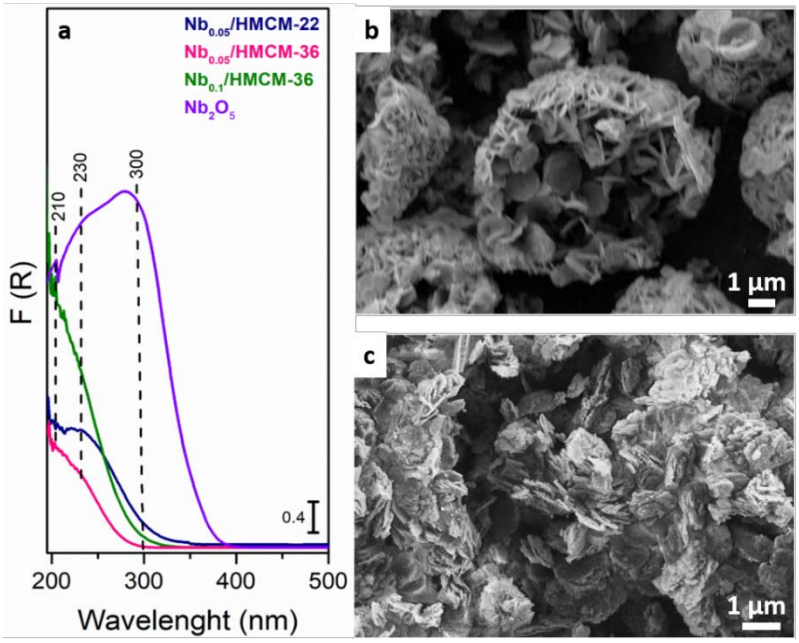

Figure 4. DR UV-Vis spectra of (a) $Nb_{0.05}$/HMCM-22, $Nb_{0.05}$/HMCM-36, $Nb_{0.1}$/HMCM-36, and Nb_2O_5. The FESEM images of (b) $Nb_{0.05}$/HMCM-22 and (c) $Nb_{0.05}$/HMCM-36.

XPS analyses were performed to obtain information about the niobium species on the surface of the zeolites. Table 2 shows the binding energies (BE) values of Nb 3d for the synthesized materials, and all samples presented BE typical of Nb(V) species. The BE of synthesized materials shifted to higher values when compared to the bulk crystalline Nb_2O_5 sample (BE = 207.1 eV), which indicates the formation of Nb species in different neighbourhoods (Si–O–Nb) [21]. Moreover, $Nb_{0.05}$/HMCM-22 and $Nb_{0.1}$/HMCM-36 presented BE near that of the crystalline Nb_2O_5 sample, 207.6 and 207.4 eV, respectively; which suggests the presence of extra framework Nb_2O_5 on both materials. Hence, all synthesized samples presented very small signals at BE = ~206 eV, which could be assigned as Nb(IV) from highly amorphous Nb_2O_5 species [28].

X-ray absorption spectroscopy was performed to assess the electronic properties and local structure of Nb atoms in the bulk. XANES spectra (Figure 5) for the Nb-impregnated MWW materials show that Nb atoms are in similar local environment once both pre-edge peak and absorption edge resemble in all spectra with slight differences. The position of the absorption edge (~19003 eV), due to 1s → 5p electronic transition [29] evidences that most of Nb atoms are pentavalent as in Nb_2O_5, which is in good agreement with XPS. The pre-edge (originated from the 1s → 4d electronic transition) is sensitive to the symmetry around the absorber atom and its intensity is more pronounced in case of

tetrahedral compounds [30]. In our case, the pre-edge intensity is compatible with that of orthorrombic Nb_2O_3, pointing out Nb atoms are in distorted octahedral coordination. It is known that water molecules can bind to Nb isomorphically substituted in silicates or dispersed on silica/alumina, increasing its coordination sphere, which could explain the pre-edge intensity in the spectra of Nb-MWW materials [31]. The XANES oscillations on the edge and post-edge do not follow perfectly those of Nb_2O_5, which could indicate that niobium atoms are present as a mixture of tetrahedrally coordinated Nb(V) and Nb_2O_5, as pointed out by UV-vis and XPS.

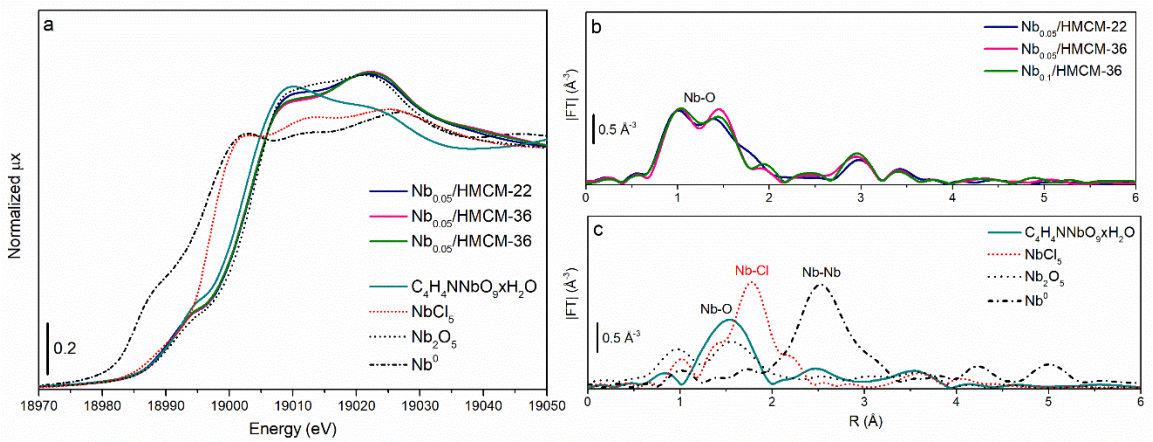

Figure 5. XAS spectra of (a) $Nb_{0.05}$/HMCM-22, $Nb_{0.05}$/HMCM-36, and $Nb_{0.1}$/HMCM-36 materials.

The morphologies of $Nb_{0.05}$/HMCM-22 and $Nb_{0.05}$/HMCM-36 materials were analyzed by FESEM and showed in Figure 4. The $Nb_{0.05}$/HMCM-22 (Figure 4b) presents larger particles formed by the agglomeration of flake-like crystallites with sizes of approximately 1.3 μm, which is typical of MCM-22 zeolite. The $Nb_{0.05}$/HMCM-36 (Figure 4c) presents the aggregation of expanded flakes-like crystallites, which suggests the increase in the distance between the MWW nanosheets occurred after pillaring. In addition, no bulk Nb_2O_5 particles were observed, poiting to Nb species in homogeneous distribution.

The TEM images in bright-field mode are shown in Figure 6. The zeolite $Nb_{0.05}$/HMCM-22 (image a) presents flat crystallites along the *ab* plane. Figure 6b reveals a set of 8 MWW nanosheets regularly stacked along the *c* plane, which confirms that the crystalline structure was preserved. Figure 6cd shows the surface of the $Nb_{0.05}$/HMCM-36 pillared material along the *ab* plane. No bulk phases of Nb_2O_5 were observed in both materials, which corroborates the good dispersion and location of Nb species between the nanosheet regions of the pillared materials.

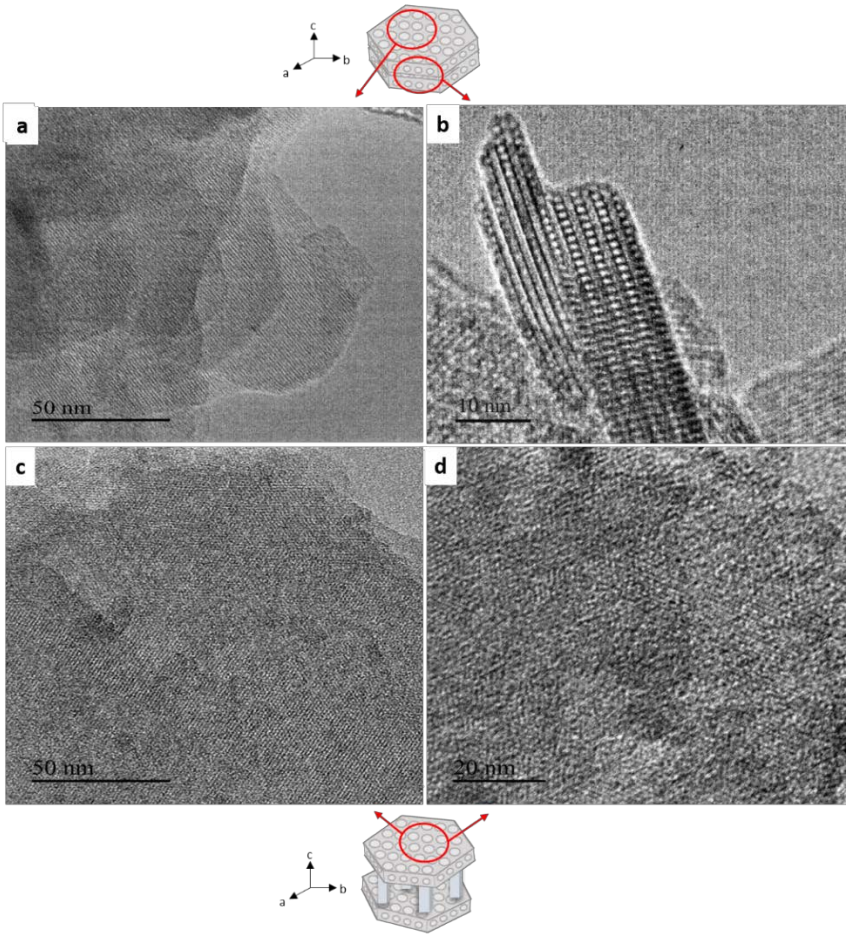

Figure 6. TEM image in bright field mode of (a), (b) $Nb_{0.05}$/HMCM-22 and (c), (d) $Nb_{0.05}$/HMCM-36 materials.

Figure 7 shows the HAADF-STEM analysis, and the single-point elemental mapping was used to examine the presence of niobium. The estimated Nb content was 4.7, 5.8, and 8.0 wt% for $Nb_{0.05}$/HMCM-22, $Nb_{0.05}$/HMCM-36, $Nb_{0.1}$/HMCM-36, respectively, which is close to the obtained by ICP. In addition, no dense phases of crystalline Nb_2O_5 were observed, which supports the good dispersion of Nb on the synthesized materials.

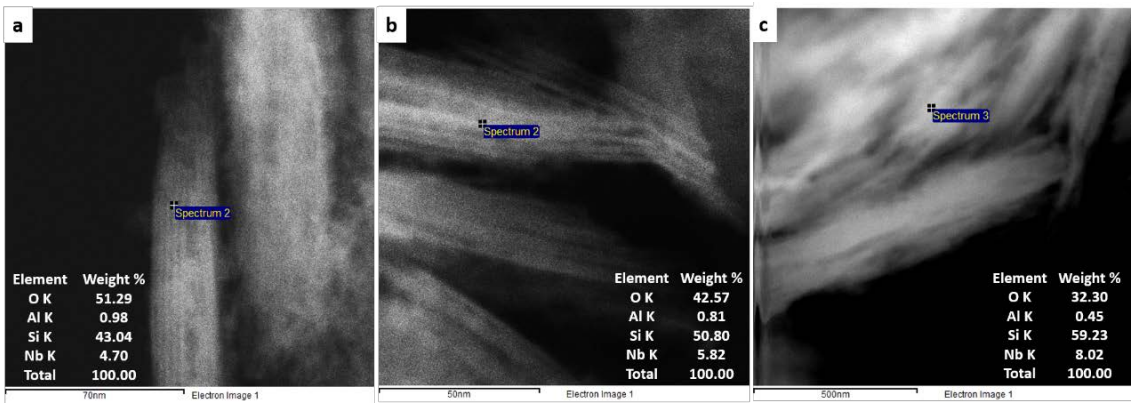

Figure 7. HAADF-STEM images with point elemental mapping of (a) $Nb_{0.05}$/HMCM-22, (b) $Nb_{0.05}$/HMCM-36, and (c) $Nb_{0.1}$/HMCM-36.

The type of acidic centers on $Nb_{0.05}$/HMCM-22 and $Nb_{0.05}$/HMCM-36 materials were characterized by IR spectroscopy with the adsorption of Py and shown in Figure 8. The spectra of the vibration of hydroxyl groups of the $Nb_{0.05}$/HMCM-22 reveal three main bands at ~3745 cm^{-1} (external silanol groups), 3730 cm^{-1} (internal silanol groups), and 3620 cm^{-1} assigned to acidic hydroxyl groups (Al–OH–Si) [23]. For the $Nb_{0.05}$/HMCM-36, the decreasing of the 3620 cm^{-1} band, and the increasing and widening of the band at 3745 cm^{-1} confirm the incorporation of additional silica in the pillared material.

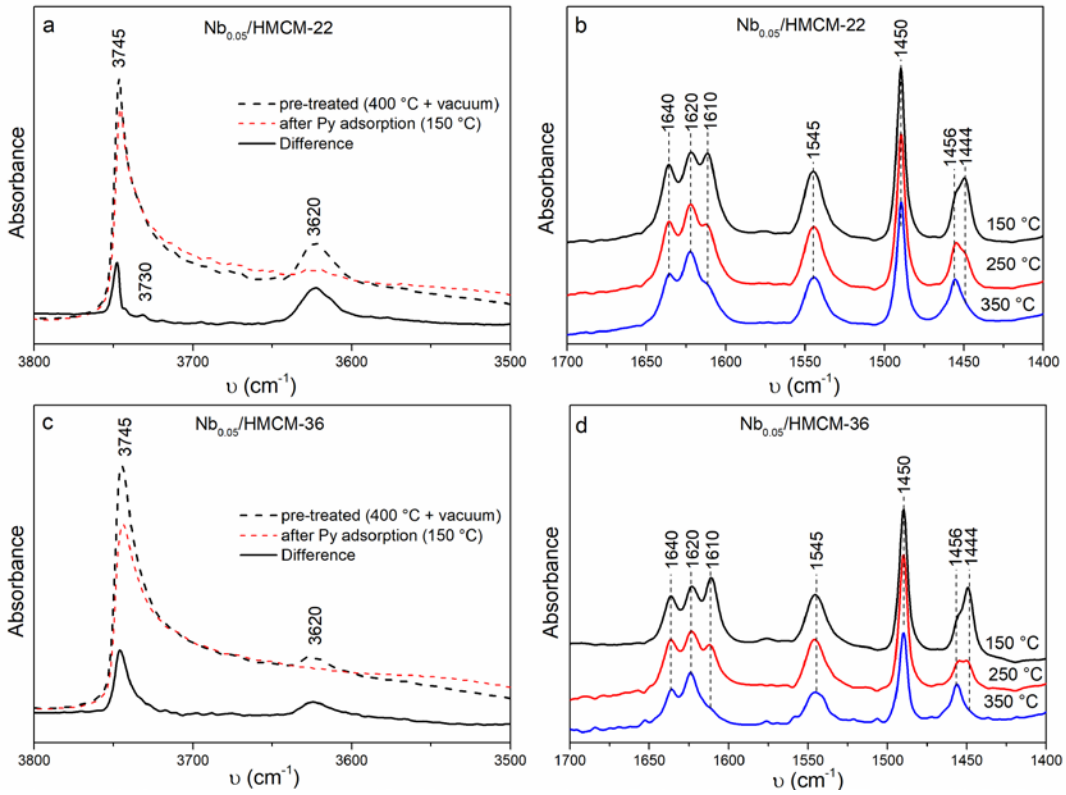

Figure 8. Spectra of the hydroxyl regions of (a) $Nb_{0.05}$/HMCM-22 (c) $Nb_{0.05}$/HMCM-36 after Py adsorption. Spectra of pyridine adsorption at 150, 250 and 350 °C of (b) $Nb_{0.05}$/HMCM-22 and (d) $Nb_{0.05}$/HMCM-36 samples.

The vibrations of Py on the Brønsted centers (PyH^+) appear at 1620, 1640 and 1550 cm^{-1}; the vibrations of Py adsorbed on Lewis centers (PyL) are assigned to the bands at 1450 and 1610 cm^{-1}. The vibration at 1450 cm^{-1} is characteristic of both PyH^+ and PyL centers. The signal at 1444 cm^{-1} is assigned to the H-bond between Py and the hydroxyl groups on the zeolite surface [23]. The spectra reveal that both materials exhibited Brønsted and Lewis acidic character. The low intensities of the $Nb_{0.05}$/HMCM-36 compared to the $Nb_{0.05}$/HMCM-22 result from the dilution of acidic centers by incorporating silica pillars.

Moreover, the band at 1610 cm^{-1} is well visible in the spectra of $Nb_{0.05}$/HMCM-22 and $Nb_{0.05}$/HMCM-36; and no observable in pure MCM-22 and MCM-36 materials [32], which suggest the generation of new Lewis centers after the Nb impregnation. Hence, the decrease of this band with the temperature increases indicates Lewis centers with moderated strength. Furthermore, the high intensity of the overlapped signal at 1444 cm^{-1} of the pillared material was related to the additional hydroxyl groups (Si-OH and/or Nb-OH) located in pillars.

Since Brønsted and Lewis acidity are related to the framework (FAL) and extra-framework (EFAL) aluminium species, respectively, ^{27}Al MAS NMR analysis of the pillared $Nb_{0.05}$/HMCM-36 is shown in Figure S1. The spectrum reveals that most Al atoms assume framework positions. The signal at 50 ppm (FAL) dominates the spectrum, and its intensity was 75% higher than the EFAL signal at 0 ppm.

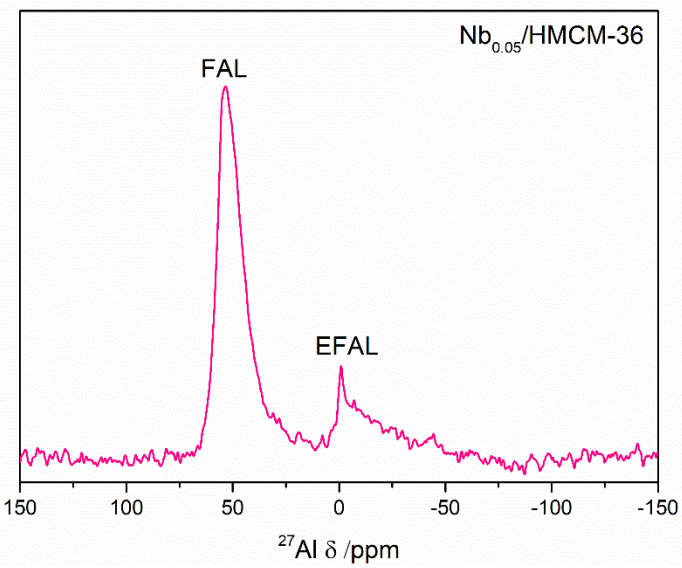

Figure S1. ^{27}Al MAS NMR spectra of $Nb_{0.05}$/HMCM-36 sample.

The obtained materials were generalized in Figure 9. After calcination of the MCM-22(P), ion exchanging for its protonic form (H^+) and impregnation of the niobium source, the $Nb_{0.05}$/HMCM-22 was obtained. The presence of silanol groups on the external surface of the MWW crystallites suggests the major presence of Nb species in tetrahedral coordination. Hence, the minimal presence of amorphous Nb_2O_5 species cannot be discarded. The $Nb_{0.05}$/HMCM-36 and $Nb_{0.1}$/HMCM-36 pillared materials were obtained after the intercalation of surfactants, insertion of the pillar solution (TEOS), calcination, ion exchanging (H^+) and Nb impregnation. Both materials maintained the 2D structure with mesopores between the MWW nanosheets. The high external surface after pillaring

promoted the homogeneous dispersion of Nb species in tetrahedral coordination on the silica pillars and the surface of the MWW nanosheets. As in the $Nb_{0.05}$/HMCM-22, the presence of amorphous extra-framework Nb_2O_5 species in small quantities in the pillared materials cannot be discarded.

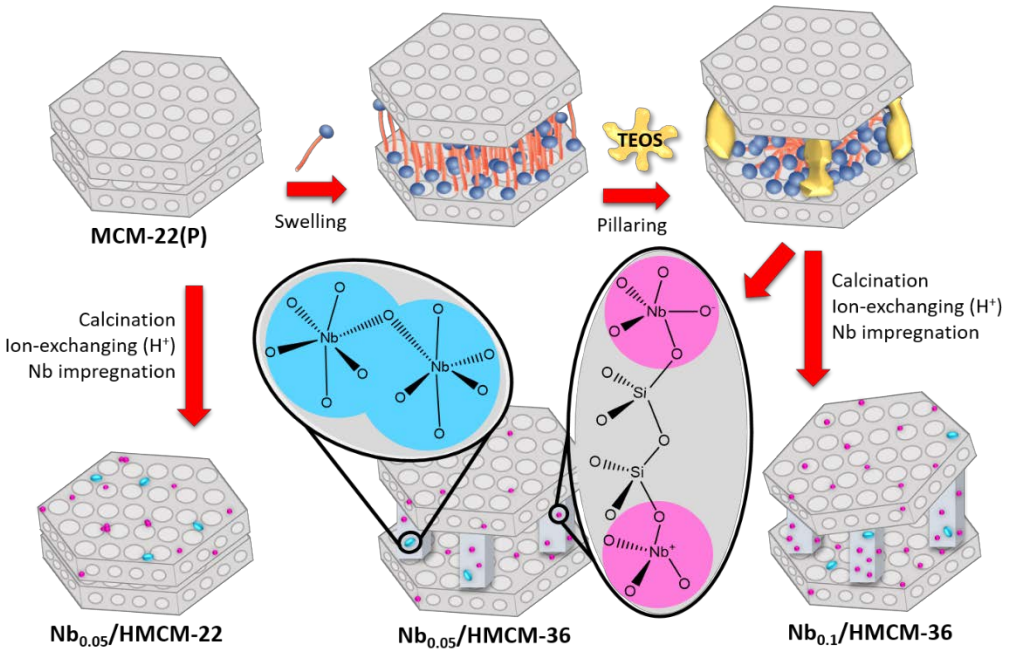

Figure 9. General scheme of the obtained $Nb_{0.05}$/HMCM-22, $Nb_{0.05}$/HMCM-36, and $Nb_{0.1}$/HMCM-36 materials.

Figure 10 exhibited the catalytic results of the oxidation of BTX. In all cases, the conversion increases with the temperature and the detected products of the reactions were only H_2O and CO_2. All studied catalysts show good BTX conversion at low temperatures; At 50 °C the $Nb_{0.05}$/HMCM-22, $Nb_{0.05}$/HMCM-36, and $Nb_{0.1}$/HMCM-36 materials present 19, 29 and 38% conversion for benzene; 12, 17 and 21% conversion for toluene; and 09, 13 and 17% conversion for o-xylene, respectively. At 300 °C the $Nb_{0.05}$/HMCM-22, $Nb_{0.05}$/HMCM-36, and $Nb_{0.1}$/HMCM-36 materials present 68, 85 and 92% conversion for benzene; 44, 62 and 69% conversion for toluene; and 36, 49 and 58% conversion for o-xylene, respectively. The results clearly demonstrate that the structure of the MWW-type materials (2D or 3D) and the niobium content influences the oxidation of BTX.

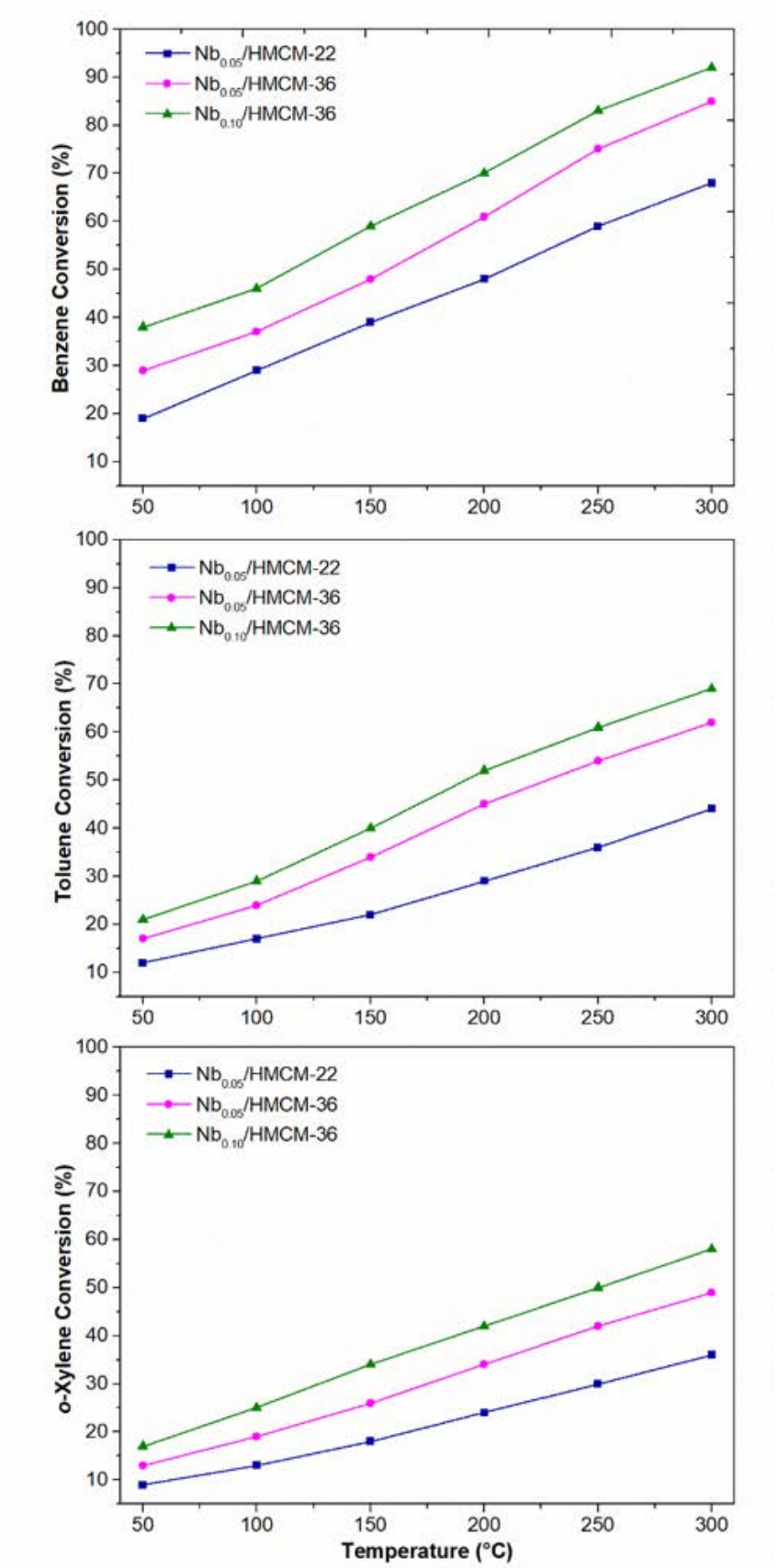

Figure 10. Catalytic oxidation of (a) benzene, (b) toluene, and (c) o-xylene as a function of temperature, using $Nb_{0.05}$/HMCM-22, $Nb_{0.05}$/HMCM-36, and $Nb_{0.1}$/HMCM-36 materials.

With similar niobium content, at 300 °C the oxidation of benzene using the $Nb_{0.05}$/HMCM-36 was 17% higher than the $Nb_{0.05}$/HMCM-22 materials. As the oxidation of VOCs are considered sensitive to reaction conditions and the structure of catalysts [19], the results confirm that the high surface area and large pore volumes of the pillared materials contributed to a better dispersion of niobium species. In addition, the mesoporous regions between the MWW nanosheets facilitate the access of the reactants to the active sites. As hydrophobic materials are benefic for the catalytic oxidation of apolar reactants, as BTX [33], it suggests the contribution of silica provided by the pillars increases the hydrophobicity of the pillared zeolites (Si/Al = 36) when compared to the zeolite $Nb_{0.05}$/HMCM-22 (Si/Al = 24). Therefore, those combined could reflect the better results of the 2D pillared zeolite compared to the 3D zeolite.

Regarding the Nb concentration on pillared zeolites, $Nb_{0.1}$/HMCM-36 showed 92% conversion of benzene, which was 7% higher than the $Nb_{0.05}$/HMCM-36 material and indicates that the increase of the niobium content in the pillared material influences the catalytic activity. The catalytic performance of $Nb_{0.1}$/HMCM-36 was even superior of the pillared MWW zeolites obtained by the insertion of the Nb source (Nb ethoxide) in the pillaring step [14]; the synthesized material with higher Nb content (14.8 %) present conversion of benzene, toluene, and o-xylene of 86, 66 and 34%, respectively, and reveals that methodology of Nb incorporation in MCM-36 influences the oxidation of BTX. The superior performance of $Nb_{0.1}$/HMCM-36 suggests that the impregnation method allows to obtain Nb species in homogeneous distribution on the surface of the pillared zeolite, while the insertion of Nb during the pillaring step could lead some occluded species inside of the pillar walls, which were not accessible to the reactants. The formation of Nb species occluded in silica walls was reported in the case of MCM-41-type materials [34].

It was assumed that the BTX total oxidation occurs by two possible pathways: via Mars-van Krevelen (MVK) and/or Langmuir-Hinshenwood (L-H). The MVK assumes that the aromatic molecules react with the lattice oxygen from the catalyst, and the oxygen from the gas phase serves to regenerate the reduced catalyst. According to the literature, this mechanism is preferential if the metal occupies extra-framework position because the Nb reducibility is easier than the framework Nb species [35]. It infers that the reduction of the catalyst Nb(V) to Nb(IV) could occur preferentially on the extra-framework octahedral Nb_2O_5 species of the synthesized materials. Indeed, Nb^{4+} species are reported from highly amorphous Nb_2O_5 material [28].

On the other hand, Nb(V) belongs to hardly reducible species, however its reducibility could be enhanced by its isolation in silica matrices [21]. Moreover, all synthesized materials exhibited isolated tetrahedral Nb(V) species in the majority. It was established that oxidizing properties of supports containing tetracoordinated Nb species are the result of dehydroxylation during calcination, which generates Lewis acid center/oxygen vacancy (Nb^{+}) and an active oxygen ($Nb\text{-}O^{-}$) [36], as presented in the pink circles in Figure 9. The first one acts as an electron trap, and the latter one has higher mobility and is easily activated than the lattice oxygen, considered active in electron transfer, and important in partial oxidation processes [37]. The formation of new Lewis centers from Nb impregnation was confirmed by IR spectroscopy with adsorbed pyridine. Moreover, the increases of the BTX conversion with the increases of Nb content on pillared zeolites could be explained by the high concentration of $Nb\text{-}O^{-}$ that promoted the easier release of oxygen. Moreover, the role of FAL and EFAL species as adsorption sites should be included. As the BTX molecules could be adsorbed and activated on both Nb and Al sites, it was suggested that the reaction follows a dual-site Langmuir-Hinshelwood model [20].

The conversion of benzene as a function of time was evaluated for the $Nb_{0.1}$/HMCM-36 and shown in Figure 11. The decreasing of the catalytic activity was not detected until the studied period (30 h), which confirms the stability of the catalyst.

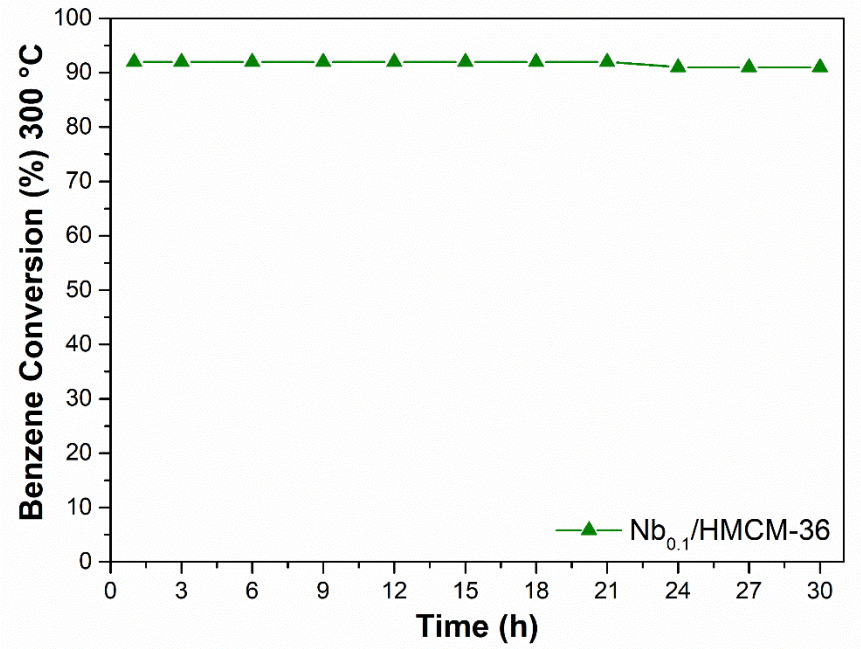

Figure 11. Catalytic oxidation of benzene as a function of time using $Nb_{0.1}$/HMCM-36 material.

4. CONCLUSION

Nb was successful incorporated into MCM-36 nd into MCM-22 via impregnation methodology. Most Nb species assumed tetrahedral coordination in pentavalent state on the external surface of the MWW-type materials, together with a minimal contribution of Nb species in extra-framework positions. The introduction of Nb generates new Lewis acidic sites in both pillared MCM-36 and tridimensional MCM-22 zeolites. The pillared zeolites exhibited a higher specific surface, larger pore volumes, and a combined micro/mesoporous structure when compared to the MCM-22 zeolite. All synthesized materials were active for BTX oxidation generating only CO_2 and H_2O as products. The more open structure of pillared zeolites promoted the good dispersion of Nb species, improving the accessibility of reactants to the active sites, which was manifested as higher BTX oxidation. The best performance was reached with the pillared zeolite impregnated with Nb 10 wt%, reaching BTX conversion at 300°C of 92, 69, and 58%, respectively. The stability of the catalyst for the oxidation of benzene at 300 °C was evaluated, and no significant loss of activity was observed after 30 h of reaction.

ACKNOWLEDGMENTS

A.J.S. thanks the Cordenação de Aperfeiçoamento de Pessoal de Nível Superior – Brasil (CAPES) – Finance Code 001, and the PPGQ-UFRGS. C.W.L. thanks PRH 50.1 – ANP/FINEP Human Resources Program for the Visiting Researcher Fellowship. This research used resources of the Advanced Photon Source, an Office of Science User Facility operated for the U.S. Department of Energy (DOE) Office of Science by Argonne National Laboratory and was supported by the U.S. DOE under Contract No. DE-AC02-06CH11357, and the Canadian Light Source and its funding partners.

REFERENCES:

[1] IZA, http://www.iza-structure.org/.
[2] G. M. R. Giannetto Pace, A.; Rodríguez Fuentes, G., *Zeolitas Características, Propriedades y Aplicaciones Industriales.*, Editora Innovación Tecnológica, Caracas, **1990**, p.
[3] K. Tanabe and W. F. Hölderich, *Applied Catalysis A: General* **1999**, *181*, 399-434.
[4] a) M. E. Leonowicz, J. A. Lawton, S. L. Lawton and M. K. Rubin, *Science* **1994**, *264*, 1910-1913; b) U. Diaz and A. Corma, *Dalton T.* **2014**, *43*, 10292-10316.

[5] A. Corma, V. Fornes, S. B. C. Pergher, T. L. M. Maesen and J. G. Buglass, *Nature* **1998**, *396*, 353-356.
[6] A. S. Fung, S. L. Lawton and W. J. Roth in *Synthetic layered MCM-56, its synthesis and use*, *Vol.* **1994**.
[7] W. J. Roth, C. T. Kresge, J. C. Vartuli, M. E. Leonowicz, A. S. Fung and S. B. McCullen in *MCM-36: The first pillared molecular sieve with zeolite properties*, *Vol. Volume 94* Eds.: H. G. K. I. K. H.K. Beyer and J. B. Nagy), Elsevier, **1995**, pp. 301-308.
[8] a) Y. J. He, G. S. Nivarthy, F. Eder, K. Seshan and J. A. Lercher, *Microporous Mesoporous Mater.* **1998**, *25*, 207-224; b) R. Purova, K. Narasimharao, N. S. I. Ahmed, S. Al-Thabaiti, A. Al-Shehri, M. Mokhtar and W. Schwieger, *J. Mol. Catal. A: Chem.* **2015**, *406*, 159-167.
[9] W. J. Roth, B. Gil, W. Makowski, B. Marszalek and P. Eliasova, *Chem. Soc. Rev.* **2016**, *45*, 3400-3438.
[10] a) J.-O. Barth, J. Kornatowski and J. A. Lercher*, *J. Mater. Chem.* **2002**, *12*, 369-373; b) J.-O. Barth, A. Jentys, E. F. Iliopoulou, I. A. Vasalos and J. A. Lercher, *J. Catal.* **2004**, *227*, 117-129.
[11] F. Jin, S. Huang, S. Cheng, Y. Wu, C.-C. Chang and Y.-W. Huang, *Catal. Sci. Technol.* **2015**, *5*, 3007-3016.
[12] C. F. Cogswell, T. P. Nigl, A. Stavola, A. Wolek, Y. Wang, J. Zummo, Y. Lin, L. Dukaye, R. Chinn and S. Choi, *Microporous Mesoporous Mater.* **2019**, *280*, 151-156.
[13] A. Wojtaszek-Gurdak, M. Zielinska and M. Ziolek, *Catal. Today* **2019**, *325*, 89-97.
[14] A. J. Schwanke, R. Balzer, C. Wittee Lopes, D. Motta Meira, U. Díaz, A. Corma and S. Pergher, *Chemistry – A European Journal* **2020**, *26*, 10459-10470.
[15] F. Jin, T.-H. Lin, C.-C. Chang, B.-Z. Wan, J.-F. Lee and S. Cheng, *RSC Advances* **2015**, *5*, 61710-61718.
[16] J. Hidalgo-Carrillo, D. Švadlák, R. Bulánek, P. Čičmanec, M. Setnička, N. L. Drenchev and P. Eliášová, *Ind. Eng. Chem. Res.* **2015**, *54*, 2030-2039.
[17] S. S. Al-Khattaf, S. A. Ali, A. M. Aitani, K. J. Al-Nawad, C.-H. Chiu and T. C. Tsai, *Applied Catalysis A: General* **2016**, *514*, 154-163.
[18] I. Kaskow, A. Wojtaszek-Gurdak and I. Sobczak, *Catal. Today* **2020**, *354*, 123-132.
[19] M. S. Kamal, S. A. Razzak and M. M. Hossain, *Atmos. Environ.* **2016**, *140*, 117-134.
[20] C. He, J. Cheng, X. Zhang, M. Douthwaite, S. Pattisson and Z. Hao, *Chem. Rev.* **2019**, *119*, 4471-4568.
[21] M. Ziolek and I. Sobczak, *Catal. Today* **2017**, *285*, 211-225.
[22] A. Corma, C. Corell and J. Pérez-Pariente, *Zeolites* **1995**, *15*, 2-8.
[23] A. Wojtaszek-Gurdak and M. Ziolek, *RSC Advances* **2015**, *5*, 22326-22333.
[24] S. Brunauer, P. H. Emmett and E. Teller, *J. Am. Chem. Soc.* **1938**, *60*, 309-319.
[25] J. O. C. S. M. Heald, D. L. Brewe, R. A. Gordon,, *Nucl. Instrum. Methods Phys. Res., Sect. A* **2007**, *582*, 2.
[26] B. R. M. Newville in *ATHENA, ARTEMIS, HEPHAESTUS: data analysis for X-ray absorption spectroscopy using IFEFFIT*, *Vol. 12* J. Synchrotron Rad., **2005**.
[27] M. Shamzhy, B. Gil, M. Opanasenko, W. J. Roth and J. Čejka, *ACS Catalysis* **2021**, *11*, 2366-2396.
[28] H. T. Kreissl, M. M. J. Li, Y.-K. Peng, K. Nakagawa, T. J. N. Hooper, J. V. Hanna, A. Shepherd, T.-S. Wu, Y.-L. Soo and S. C. E. Tsang, *J. Am. Chem. Soc.* **2017**, *139*, 12670-12680.
[29] A. Froideval, C. Degueldre, C. U. Segre, M. A. Pouchon and D. Grolimund, *Corros. Sci.* **2008**, *50*, 1313-1320.
[30] M. Massa, A. Andersson, E. Finocchio and G. Busca, *J. Catal.* **2013**, *307*, 170-184.
[31] C. Tiozzo, C. Bisio, F. Carniato, A. Gallo, S. L. Scott, R. Psaro and M. Guidotti, *Phys. Chem. Chem. Phys.* **2013**, *15*, 13354-13362.
[32] A. J. Schwanke, S. Pergher, U. Díaz and A. Corma, *Microporous Mesoporous Mater.* **2017**, *254*, 17-27.
[33] A. J. Schwanke, R. Balzer and S. Pergher in *Chapter 49 - Mesoporous Materials for Reduction of Air Pollutants: Volatile Organic Compounds*, (Ed. C. Mustansar Hussain), Elsevier, **2018**, pp. 908-915.

[34] M. Ziolek, I. Nowak, B. Kilos, I. Sobczak, P. Decyk, M. Trejda and J. C. Volta, *J. Phys. Chem. Solids* **2004**, *65*, 571-581.
[35] S. I. Ziolek M., Trejda M., Wojtaszek-Gurdak A. in *Structure and Reactivity of Zeolites Containing Group Five Elements (V, Nb, Ta)*, *Vol. 178* (Ed. S.-S. M. Pérez Pariente J.), Springer, Switzerland, **2017**.
[36] M. Ziolek, *Catal. Today* **2003**, *78*, 47-64.
[37] a) B. Kilos, M. Aouine, I. Nowak, M. Ziolek and J. C. Volta, *J. Catal.* **2004**, *224*, 314-325; b) Y. Qin, H. Wang, C. Dong and Z. Qu, *J. Catal.* **2019**, *380*, 21-31.